Aerospace Science and Technology 168 (2026) 111160

Contents lists available at ScienceDirect

Aerospace Science and Technology

journal homepage: www.elsevier.com/locate/aescte

Original article

Development of neuromorphic event-based imaging spectroscopy for hypersonic flight observation

Tamara Sopek [a,1,*], Fabian Zander [b,2], Byrenn Birch [b,3], David Buttsworth [b,4]

[a] The University of Queensland, Brisbane, QLD, 4072, Australia
[b] University of Southern Queensland, Toowoomba, QLD, 4350, Australia

ARTICLE INFO

Cummings Russell

Keywords:
Hypersonics
Event-based
Spectroscopy
Observation
Flight event
High-speed

ABSTRACT

Enhanced capability to collect vital hypersonic flight data is required to better understand the physics of the flow around spacecraft entering Earth's atmosphere. Daytime recording, while possible, remains particularly challenging and often requires compromises due to saturation and noise in this environment. Using novel, bio-inspired event-based cameras allows spectral measurements to be performed equally well during both day and night, without modifications to instrumentation - overcoming a major current limitation associated with daytime tests. Combining these cameras with high-resolution spectroscopy enables more reliable collection of critical data, such as temperature and species composition in the flow around re-entering spacecraft. Measurements were performed using a novel neuromorphic spectroscopy system and a range of light sources. These tests were conducted in the 400–900 nm spectral region to match the operational range of the event-based camera. The acquired data show that both broadband and discrete line spectra were obtained. Results for dynamic range, daytime performance, and long-range spectroscopy demonstrate improved performance of the event-based system compared to the conventional cameras typically used under similar conditions. This work demonstrates, for the first time, that a spectroscopy system based on neuromorphic technology is capable of successfully recording emission spectra. These results represent a landmark step toward developing advanced spectroscopy diagnostics for hypersonic flight observation, including Earth re-entry missions.

1. Introduction

Visual, photo- and videographic information of hypersonic and space flight events has played a crucial role in assessing performance, verifying successes and documenting failures [1,2]. Forensic analysis of photographic records from rocket failures - including those from the Space Shuttle disasters (Challenger and Columbia) - has contributed to improved system design [3,4]. Videography of SpaceX successful launches and landings has helped increase interest in rocketry over the past decade, while footage of failures led to rapid system improvements [5,6].

This becomes especially important as the next 20 years are expected to focus on human travel to other planets, particularly Mars [7]. A human-crewed mission to Mars will differ significantly from previous robotic missions by including a return trip, further amplifying the technological challenges [8].

For instance, despite extensive research and progress, considerable uncertainties remain in modeling heat shield performance-primarily due to challenges in accurately predicting radiative heat transfer in hypervelocity flight regimes [9]. During a Mars return mission, the spacecraft will experience velocities higher than those of any previous Earth re-entry vehicle, resulting in extreme radiative and convective heating during re-entry and deceleration [10,11].

A heat shield based on current technology would become unacceptably heavy. For a robotic mission, this directly translates to a lower payload mass fraction; for a human mission, it could limit the number of crew members. Significant advancements in heat shield modeling are required to reduce mass, enabling the design of safer and more efficient

* Corresponding author.
E-mail address: t.sopek@uq.edu.au (T. Sopek).
[1] Postdoctoral Research Fellow.
[2] Associate Professor.
[3] Senior Lecturer.
[4] Professor.

https://doi.org/10.1016/j.ast.2025.111160
Received 23 September 2025; Received in revised form 8 October 2025; Accepted 25 October 2025
Available online 7 November 2025

Nomenclature

AER	Address-Event Representation
EB	Event-Based
FoV	Field of View, °
fps	Frames per second
L_v	Luminance, cd/m^2
OES	Optical Emission Spectroscopy
SNR	Signal to Noise Ratio
f	Focal length, mm

spacecraft with higher payload mass fractions-thus improving the feasibility of such missions.

Thus, there is a strong incentive to better characterize the conditions experienced during hypersonic flight [12]. However, the only two options for generating realistic aerothermodynamic conditions to study these phenomena are high-speed ground test facilities or flight experiments [13]. Although ground test facilities [14–16] are very effective at replicating individual aspects of high-speed flows, it is not possible to fully recreate the actual flight environment. The only way to achieve this is through rare and expensive flight testing.

As a result, researchers typically conduct a series of much cheaper tests in ground facilities as an initial stage, followed by more costly flight tests [17]. Remote observations of high-speed flight events present the best opportunity to obtain high-quality radiation data, while avoiding the need to embed sensors and additional hardware onto the vehicle. For objects such as capsules and rockets, this eliminates the penalty of added mass and system complexity. In the case of natural objects such as meteorites and asteroids, embedding sensors is not an option-making remote observation the only viable method for acquiring data on aerothermodynamics and spacecraft demise processes, which are crucial for modeling the hazards associated with debris fields [18].

While several researchers have conducted ground-based observations [19–21], besides the UniSQ group [22–25], the NASA SCIFLI team is the only other civilian group regularly performing airborne observations [26–28]. This further limits the availability of high-quality data, which directly affects the progress of science based on such measurements.

Additional challenges in data collection arise from issues specific to each type of observation. In ground-based observations, a major drawback is the significant atmospheric absorption of radiation. Moreover, many relevant events occur over the ocean, making ground-based observations impossible.

While airborne observations can address the issues of atmospheric absorption and ocean coverage-by bypassing cloud interference and improving accessibility-they still face the problem of sky background brightness. Commonly used CCD and CMOS cameras struggle under these conditions. Although such cameras can record objects against a clear blue sky, doing so is difficult and requires compromises due to saturation and noise in this environment.

As a result of these overall challenges in hypersonic flight measurements-compounded by limitations in the imaging technologies typically used - high-quality spectroscopic data remain scarce. To maximize the collection of valuable data from every hypersonic flight event, the goal of this study was to explore recent advancements in vision technology and assess their potential advantages over standard cameras for remote observations of high-speed flight events.

Neuromorphic event-based (EB) vision is a novel technology that offers significant advantages in sensor performance compared to conventional cameras, as illustrated in Fig. 1. Typical hypersonic flight scenarios are shown, ranging from rocket launches and spacecraft re-entry to meteor showers, with imaging characteristics of both standard CCD and EB cameras indicated.

CCD cameras, which produce frame-based output dependent on exposure settings and limited by low temporal resolution, encounter challenges when imaging fast-moving objects or scenes with bright backgrounds. In space imaging, they also struggle with high data transfer rates caused by large amounts of low-importance information, such as empty space.

In contrast, EB cameras are better suited for space-oriented imaging, offering continuous data streams with high temporal resolution and low data rates, as they capture only changes in the scene-resulting in a small amount of highly relevant information. Due to their high dynamic range, measurements using this technology can be performed equally well during both day and night without any modifications to the instrumentation.

Recently, interest has grown in exploiting these capabilities for scientific studies; however, the characteristics of EB cameras make their response is inherently non-linear. This highlights the need for new data processing and simulation methods that are capable of addressing this complex behaviour. Different approaches have been implemented to model EB cameras' response, with new models being developed continuously and including complex algorithms and neural networks [29–33].

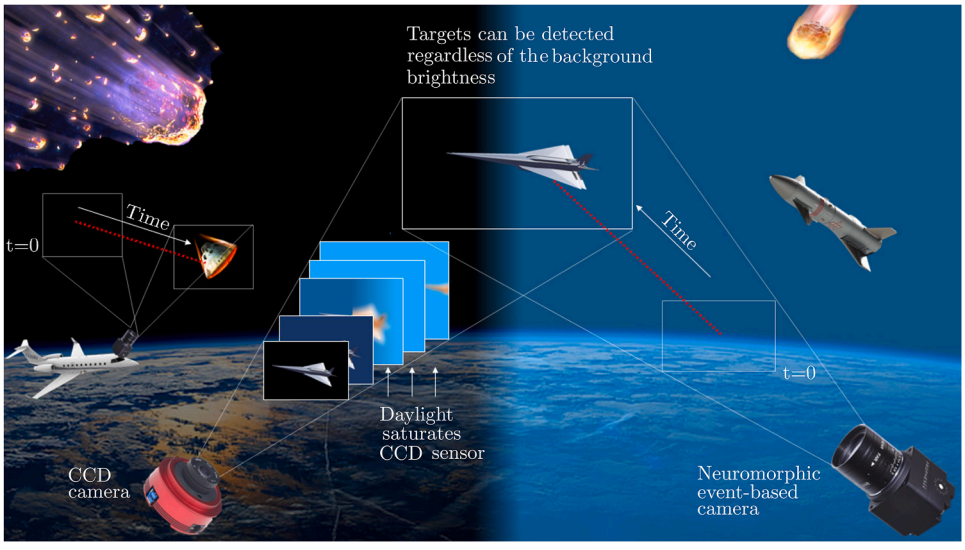

Fig. 1. Event-based space imaging compared to the standard CCD sensor approach. Adapted from Afshar [34].

The capability to perform well during both day and night enables easier detection and tracking of targets in the space environment and has been successfully used for such purposes previously [34]. Our proposed instrument is novel in that it couples an EB camera with a spectrometer to perform neuromorphic imaging spectroscopy-an approach that has never been trialed before.

This study is motivated by the need to advance critical airborne remote diagnostics of hypersonic and space flight. The results presented here represent an essential first step toward developing such capabilities. This paper reports on efforts to develop a state-of-the-art optical spectroscopy technique that enables more flexible, cost-efficient, and responsive diagnostics for collecting invaluable hypersonic and space flight data through remote observations.

The proposed system will enhance the collection of radiation spectroscopic data under all lighting conditions-from daytime to nighttime-representing a significant advancement in optical sensor capability. The expected outcome is a new method that:

1. Allows acquisition of extremely rare and valuable information about the flow field of hypervelocity flight vehicles (e.g., temperature and species composition) with a higher likelihood of data capture than is possible with current technology; and
2. Enables daytime measurements, a capability that is extremely challenging with standard cameras.

Analysis of the acquired data will provide temperature and species composition information for heat shields, which will be used to develop theoretical models (e.g., for re-entry aerothermodynamics and spacecraft or meteor disintegration), augment existing databases, and benchmark both ground-based experiments and numerical simulations.

The availability of a novel, non-intrusive diagnostic capability for monitoring hypersonic and space flight events will contribute to improved safety, greater reliability, and a deeper understanding of these phenomena. Ultimately, the availability of additional flight data will support the development of advanced spacecraft designs.

To this end, radiation measurements were conducted to produce a benchmark dataset using a neuromorphic optical spectroscopy system. A newly developed system was used to monitor radiation from various light sources at both short (millimeter-scale) and long (kilometer-scale) distances. The captured radiation data falls predominantly within the visible spectral range (approximately 400–900 nm), which corresponds to the sensitivity range of the cameras currently available to the authors.

While numerous studies have explored aspects of event-based imaging, none to date have addressed the specific conditions, methodologies, and data presented in this work, making it a novel and distinct contribution to the field.

2. Event-based (EB) cameras

EB cameras are novel dynamic vision devices inspired by the human retina that represent “a paradigm shift in the way visual information is acquired” [35]. Commonly known as neuromorphic imagers, these cameras record only when there is a change in light intensity within the field of view. Instead of continuously measuring absolute brightness, they respond asynchronously and independently at each pixel to changes in brightness within the scene.

These devices represent an emerging hardware capability, and their advanced method of data acquisition has enabled successful application across a wide range of fields-from robotics [36], to object and gesture recognition [37], to particle velocimetry [38]. The most relevant application for this work is their use in star tracking and mapping [34,39]. Because they do not continuously record data, the issue of handling vast amounts of information when imaging largely empty space is avoided.

Additionally, since they detect only changes in light intensity, EB cameras can operate effectively across a wide range of illumination conditions. As a result, target detection and recording are possible regardless of background brightness, and imaging performance remains consistent during both day and night without any modification to the sensors.

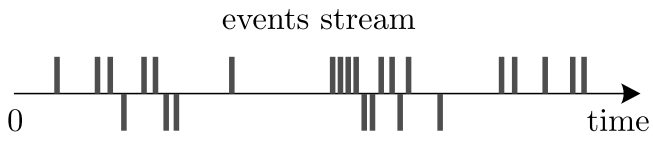

Fig. 2. Events stream output of the EB camera.

Principle of operation of event-based cameras

While a traditional camera outputs frames at fixed time intervals, an event-based (EB) camera outputs visual information as asynchronous events at microsecond resolution, transmitting data with sub-millisecond latency. An event is generated each time a single pixel detects a change in light intensity within the field of view (FOV). Specifically, when the change in a pixel’s luminosity exceeds a predefined threshold, it produces a visual event containing an x and y address, a timestamp, and a polarity-either “ON” or “OFF,” depending on whether the change in relative luminosity is positive or negative.

Thus, the output of an EB camera is a stream of digital “events” or “spikes” at variable frequency, with each event corresponding to a pixel’s predefined threshold of change in logarithmic light intensity at a specific point in time. In mathematical notation, the output of an EB camera is a stream of N events, e_i, as shown in Fig. 2 and expressed as:

$$e_i = [x_i, y_i, t_i, p_i]_{i=1,\ldots,N} \tag{1}$$

where x and y are the spatial coordinates in pixels, t is the timestamp of the event, and $p \in -1, 1$ is the polarity of the event (the sign of the logarithmic intensity change).

This method of encoding visual information is inspired by the spiking nature of biological visual and optic pathways. The address-event representation (AER) [40] is commonly used in neuromorphic engineering. The operating principle of the event-based pixel for the camera used in this study is shown in Fig. 3 and has been adapted from Finateu et al. [41].

After the information is transmitted from the sensor, each pixel memorizes its last log intensity and continuously monitors for a change of predefined magnitude from this memorised value. Once that change is detected and recorded, the sensor sends another event. This change, or contrast threshold, is thus defined as:

$$pC = \Delta L(x, y, t) = L(x, y, t) - L(x, y, t - \Delta t) \tag{2}$$

where C is the contrast sensitivity (typically a 10–15 % relative brightness change), $L(x, y, t) = \log(I)$ denotes the logarithm of light intensity (with base e, i.e., $\log_e$), x and y are the spatial coordinates in pixels, t is the timestamp of the event, and Δt is the time elapsed since the previous event at the same pixel. We can thus express Eq. 2 in the following form:

$$\pm C = \log\, I(u, t) - \log\, I(u, t - \Delta t) \tag{3}$$

where $u = \{x, y\}$. The logarithmic relationship represents the pixels’ response to percentage changes in illumination rather than the absolute magnitude of the change, allowing the pixels to operate over a very wide dynamic range. The proof comes from the brightness constancy assumption, which says that the intensity value of p,before and after the motion, must remain unchanged:

$$L(x, y, t) = L(x + u, y + v, t + \Delta t) \tag{4}$$

Replacing the right hand term by its first order approximation at time $t + \Delta t$ gives us:

$$L(x, y, t) = L(x, y, t + \Delta t) + \frac{\delta L}{\delta x} u + \frac{\delta L}{\delta y} v \tag{5}$$

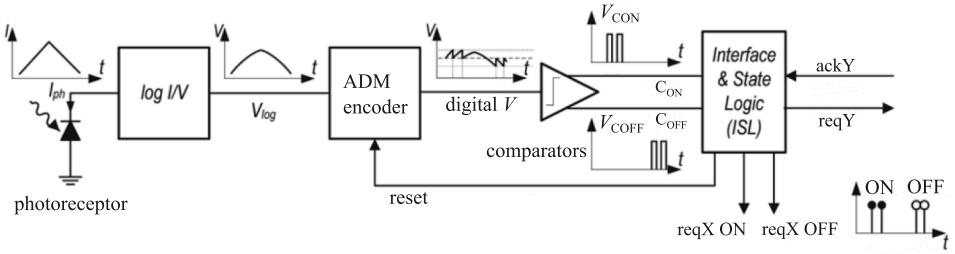

Fig. 3. Pixel block diagram, adapted from Finateu et al. [41].

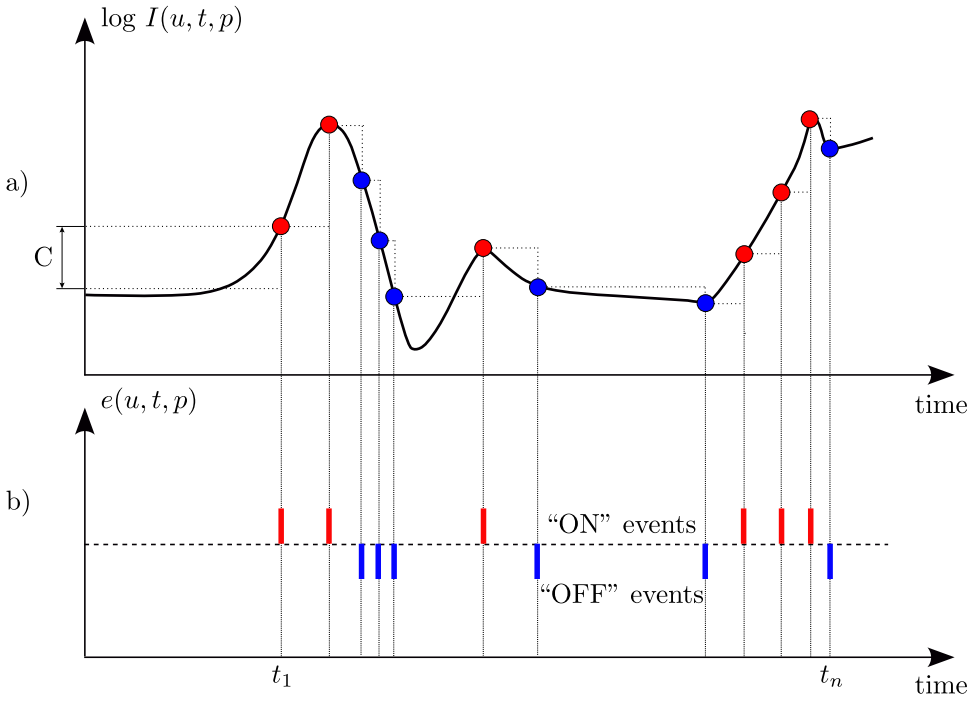

Fig. 4. Generative event model.

By rearranging this, we obtain:

$$L(x,y,t+\Delta t) - L(x,y,t) = -\frac{\delta L}{\delta x}u - \frac{\delta L}{\delta y}v \tag{6}$$

Finally, we get:

$$\Delta L = C = -\nabla L \cdot u \tag{7}$$

The generative event model is illustrated in Fig. 4.

EB cameras transmit events from the pixel array to the periphery and subsequently out of the camera using a shared digital readout pipeline. A schematic of the simplified readout process for the camera used in this study, the Prophesee IMX636, is shown in Fig. 5.

Asynchronous EB pixel arrays are based on the idea that a significant portion of the information conveyed by an event lies in its precise timing of occurrence. This is particularly important for the use of EB cameras in high-speed applications such as tracking and optical flow with kHz update rates. Thus, early timestamping of events is imperative-that is, as early as possible in the signal processing chain-to avoid any timing distortions caused by the readout process. For the camera used in this study, the typical latency for reading out a single event, from pixel firing to timestamp assignment, is approximately 60–70 ns. Pixel latency, defined as the delay between the light intensity change in the scene and contrast detection by the pixel, is typically around 200 μs.

The AER communication circuits losslessly transmit all events; however, the readout pipeline can become saturated, affecting the timing of event transmissions. In scenes with high activity, as the event detection rate increases, the readout system's limitations are reached when the event detection rate exceeds the maximum readout speed. This causes simultaneous events to queue up, resulting in increased readout latency and introducing timestamp errors. Event cameras have readout rates ranging from 2 MHz [43] to 1200 MHz [44], depending on the sensor and hardware interface. In most applications and under typical conditions, the latest generation of EB camera readout systems can handle sustained rates of at least 100–200 MHz without significant impact on timestamp accuracy.

The timing of events can be reported with very accurate temporal resolution on the order of microseconds, and visual information is no longer acquired based on an external clock (e.g., global shutter); instead, each pixel has its own sampling rate. Therefore, these sensors capture visual information predominantly in the time domain, unlike traditional frame-based cameras which provide a greater amount of spatial information. Because event-based camera pixels only detect temporal changes, time-constant information such as static background is not captured. Since this information is redundant anyway, the result is a sparser representation of the scene compared to standard cameras, allowing event-based cameras to achieve high temporal resolution with a very low data rate.

Symbolic computation has been extensively used in interpretation and analysis of EB camera data. Recongised patterns are translated into symbolic assertions. In other words, abstract, structured sym-

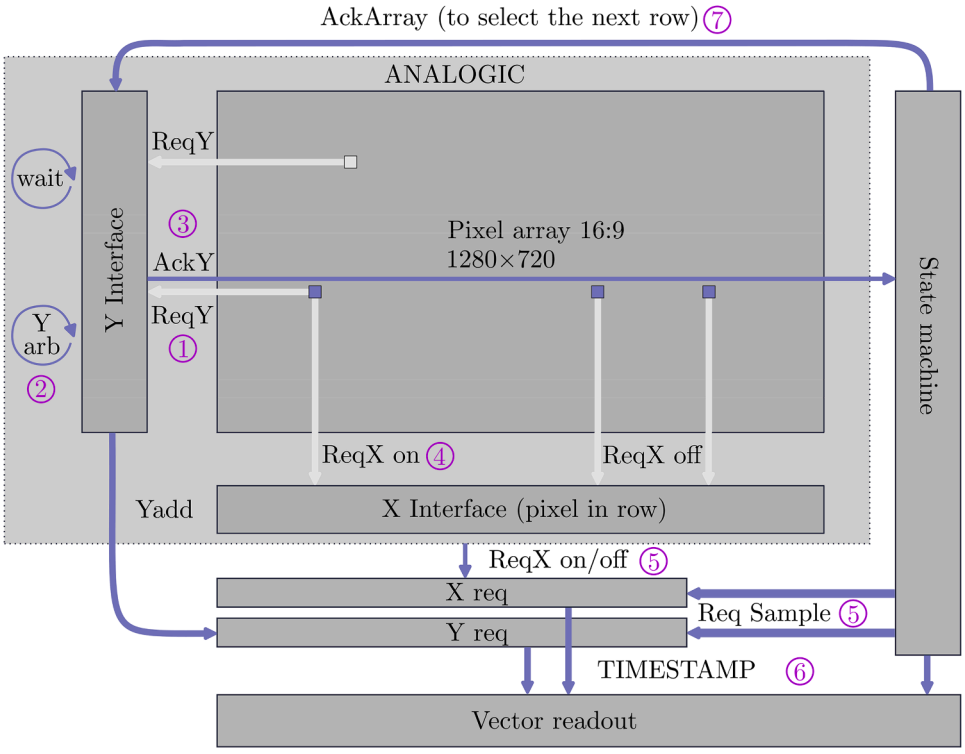

Fig. 5. Simplified readout process, adapted from S.A. [42].

bols (eg. `gesture(raise_hand)`, `approaching(car, crosswalk)`, `enters_zone(person1, zoneA)`) from the raw event streams captured by EB cameras. Next, symbolic reasoning is applied to reconstruct processes (eg. `IF gesture(user, wave) THEN greet(user)`). The goal of symbolic computing is to translate low-level, asynchronous sensory data into high-level, symbolic representations that can be used for reasoning, decision-making, or learning. It has been used for gesture recognition in robotics [45], autonomous driving [46], surveillance and activity recognition [47], object detection and tracking [38,48], and other applications. Symbolic computation in EB cameras enables systems to not only see fast, but also understand what they see in a structured, explainable way.

While event-based cameras do not output traditional images, it is possible to create pseudo-images by integrating the event stream over a chosen length of time. Fig. 6 shows an example of event-based camera output with and without log intensity change, created by integrating a stream of events over $\Delta t = 33$ ms. The scene depicted is a dog against a wall, with the dog moving slightly in the image on the right.

The advantages of neuromorphic event-based imaging include high dynamic range, high temporal resolution, no motion blur, low mass, low latency, low power consumption, reduced bandwidth, and significant reductions in data storage requirements. Event-based neuromorphic cameras provide capabilities that cannot be achieved using conventional scientific cameras, thus representing a game-changer in remote observations. These cameras emit data as a spatio-temporal pattern rather than using conventional frames. The sensor pixels are independent and asynchronous, with no fixed exposure times, resulting in high temporal resolution and a high dynamic range. These sensors can continuously image during motion, allowing the camera to move arbitrarily while still capturing valid data-ideal for low-stability environments such as airborne observations. Consequently, they are able to capture the object in focus and background objects without generating the streaks typically found when imaging events such as capsule re-entry or meteor showers. The high dynamic range enables the same sensor to perform equally well during both day and night without modifications to the instrument configuration.

Table 1
Comparison of event-based and selected CCD camera.

	Event-based camera (Prophesee Gen4)	Standard camera (QHY5III174)
dynamic range	high (>120 dB)	low (75.6 dB)
max fps (update rate)	high (asynchronous): >10kfps	low (synchronous): 138 fps
resolution at max fps	full-frame	full-frame
data rate	≈1 GB/s	5 GB/s
bits per event/pixel	≈40 bits/event	12 bits/pixel
weight	40 g	89 g
mean power consumption	mW	W
resolution	1280 x 720 px	1936 x 1216 px
pixel size	4.86 μm	5.86 μm
latency	low (μs)	high (ms)
motion blur	no	yes
absolute intensity	no	yes

The disadvantages of event-based imaging include the inability to use traditional vision or image processing algorithms due to asynchronous pixels and the lack of absolute light intensity information (only binary intensity changes are recorded). New methods are required to address the spatio-temporal, photometric, and stochastic nature of event data, making the analysis more complex. In cases where there is no change in light intensity, such as a static scene, no events are generated, and thus the only output is background noise. The asynchronous event readout scheme of EB cameras has a limited maximum readout speed, which can become an issue in extremely active scenes. Additionally, as these cameras are not yet mature technology and have a limited number of manufacturers, this results in lower sensor resolution, higher cost (currently, the camera used in this study is sold at €5000), and a limited knowledge base. Table 1 provides a comparison between an event-based camera and a standard camera.

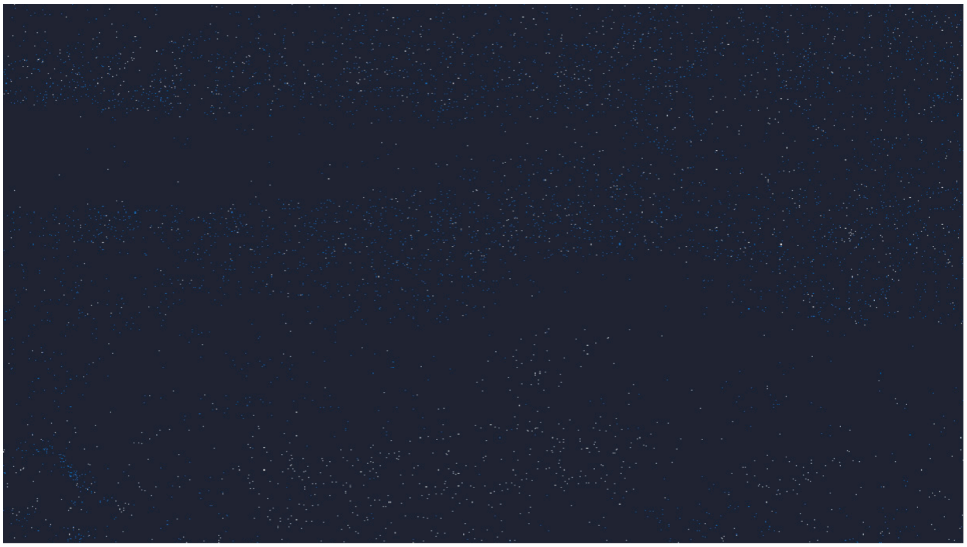

(a)

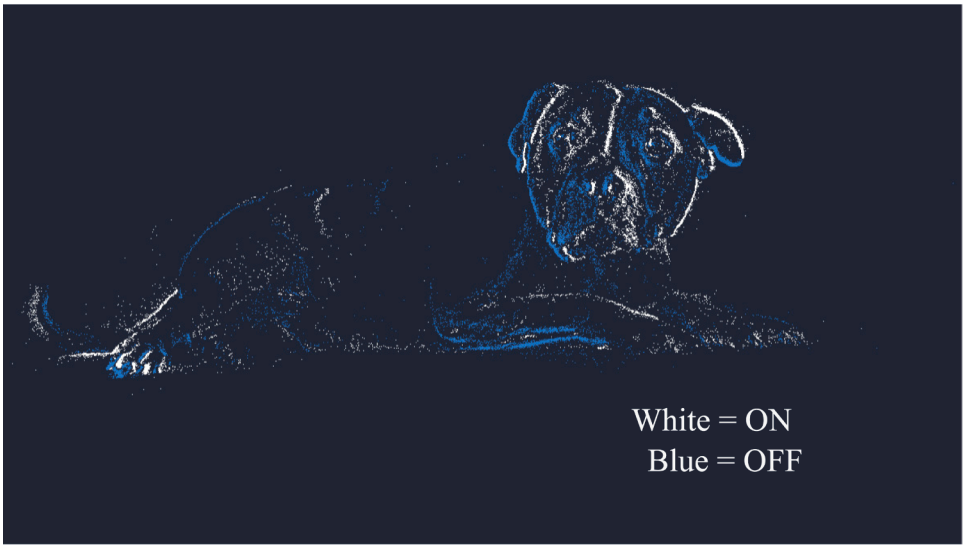

(b)

Fig. 6. Example of an event-based camera output with a) no motion and b) with motion in the scene. In b), ON and OFF events are captured where ON is increase and OFF is decrease in logarithmic light intensity.

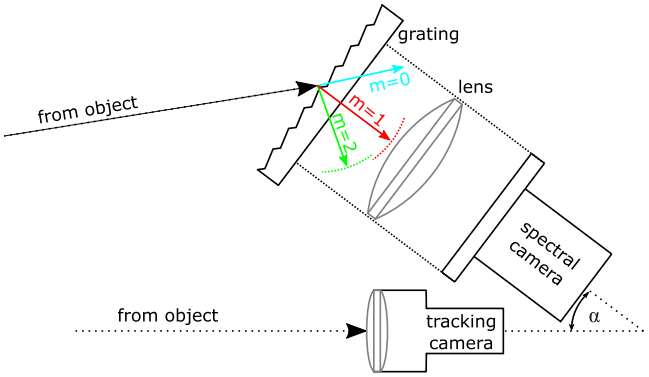

Fig. 7. Example of a slitless grating spectrometer [25].

The success achieved in using these cameras for Space Situational Awareness (SSA) [34,39] provides confidence in their potential application for the different type of space imaging proposed here. The aim of this project is to develop an optical sensor combining an event-based camera with a grism (grating + prism) slitless spectrometer for remote sensing of radiation. We are the first to couple this neuromorphic imager with a slitless spectrometer.

3. Experimental setup

An EB camera is paired with a slitless spectrometer to enable the collection of spectroscopic data. The slitless spectrometer is a well-known and commonly used method for capturing spectral emissions from phenomena such as the shock layer radiation of a sample return capsule [20,49,50] or space debris [18,51]. It typically consists of an order-sorting prism, a transmission grating, a lens, and an optional spectral filter array.

The prism refraction angle is typically chosen to redirect the center wavelength of the observed spectrum back onto the optical axis. However, the spectrometer design in this study was simplified by tilting the recording end of the system by a tilt angle α, as shown in Fig. 7. This approach allowed us to avoid including the prism while keeping the

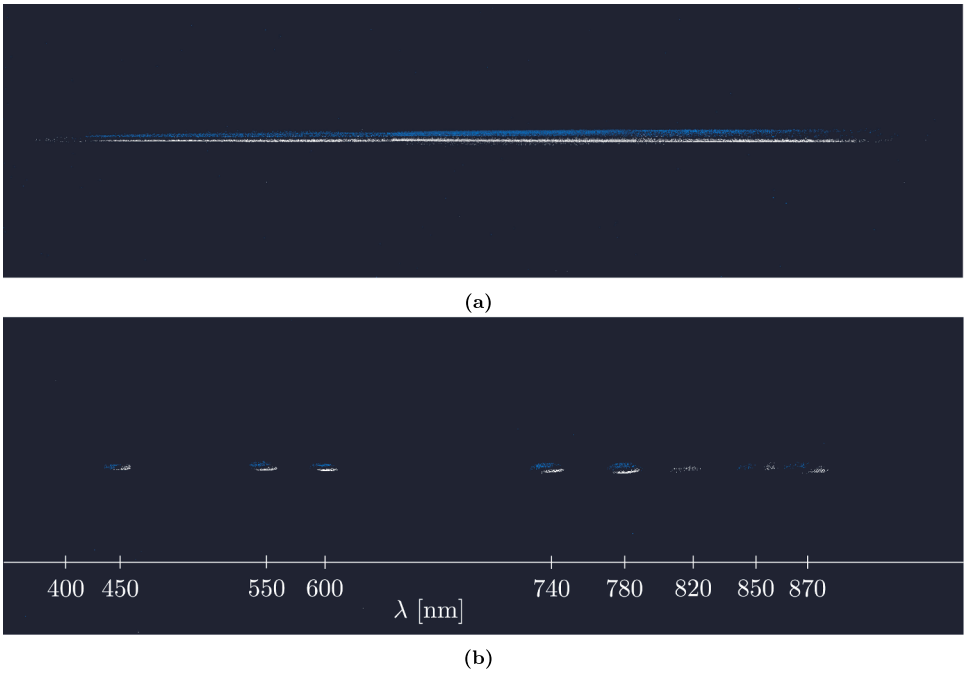

Fig. 8. Example of spectra from a broadband light source, integrating sphere: a) broadband spectrum and b) sections of broadband spectrum obtained with bandpass filters (FWHM = 10 nm).

image of the spectrum parallel to the focal plane, with all colors of the spectrum in focus simultaneously.

Experiments reported in this study were performed using a Prophesee Gen4 event-based camera with an embedded Metavision® IMX636 sensor, camera lens, transmission grating, filter, and light source. Three variations of spectrally resolved measurements were conducted using:

- Integrating sphere (Labsphere PT-038-PLS). This light source delivers a broadband spectral radiance output and was chosen for the fundamental validation of the EB system's ability to capture spectral data. With a tunable luminance level, it was also used to demonstrate the dynamic range capabilities.
- Mercury/argon lamp (Avantes AvaLight-CAL-HgAr). This spectral calibration lamp outputs radiance in the form of a discrete spectrum, i.e., spectral lines, over the 253.6–922.5 nm spectral range, covering the operational range of our EB camera system.
- Streetlight (LED-type and gas-type). These lamps are readily available light sources for long-range spectroscopy. The LED-type lamp outputs only a broadband spectrum, while the gas-type lamp typically delivers a discrete spectrum superimposed on broadband radiation.

Optical Instrumentation

The optical arrangement used in these experiments was designed to enable the recording of spectrally and spatially resolved radiation emitted from various light sources. The radiation measurements employed both an event-based camera and a standard camera system, covering a spectral range of approximately 400–900 nm. Table 2 provides details on the spectrometer properties for both the event-based and standard camera systems. The EB camera lens was changed when performing daylight and long-range spectroscopy measurements, which affected several parameters listed in Table 2, namely spectral resolution, spectral width, and field of view (FOV).

Intensity Calibration

Accurate calibration of the recorded data is a vital part of the process for all experimental measurements. All elements in the optical path, such as windows, gratings, and filters, have wavelength-dependent efficiencies with which they transmit light. Calibration of all spectral data is necessary to convert the EB camera output into standard light intensity units. However, this is not a trivial task - since EB cameras operate by recording only changes in light intensity rather than absolute intensity, these systems must be calibrated to convert the recorded data into absolute intensity values. As explained earlier, the output of EB camera systems includes only binary information about light intensity changes, unlike standard camera frames that record counts. While standard camera frames also require calibration with a known light source

Table 2
Summary of the spectrometer properties.

Instrument	THUNDER	ASTRO
sensitivity band [nm]	350–900	350–900
grating blaze angle [°]	29.87	29.87
grating [lines/mm]	830	830
camera	Prophesee Gen4	QHY5III174
sensor	Sony IMX636HD	Sony IMX174
pixel array	1280 x 720	1920 x 1200
pixel size [μm]	4.86	5.86
integration time [s]	0.033 (pseudo images)	0.033
	light sources & dynamic range[a]	
lens focal length [mm]	16	12
resolution [px nm^{-1}]	2.8	7.12
spectral width [nm]	440	270
	daylight spectroscopy[b] *	
lens focal length [mm]	50	–
resolution [px nm^{-1}]	6.2	–
spectral width [nm]	117	–
	long range spectroscopy[b]	
lens focal length [mm]	75	–
resolution [px nm^{-1}]	12.8	–
spectral width [nm]	56	–

[a] wavelength along the longer dimension of the sensor, 1280 px.
[b] wavelength along the shorter dimension of the sensor, 720 px.

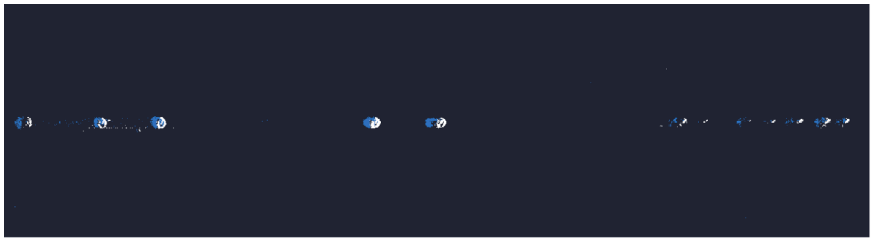

(a)

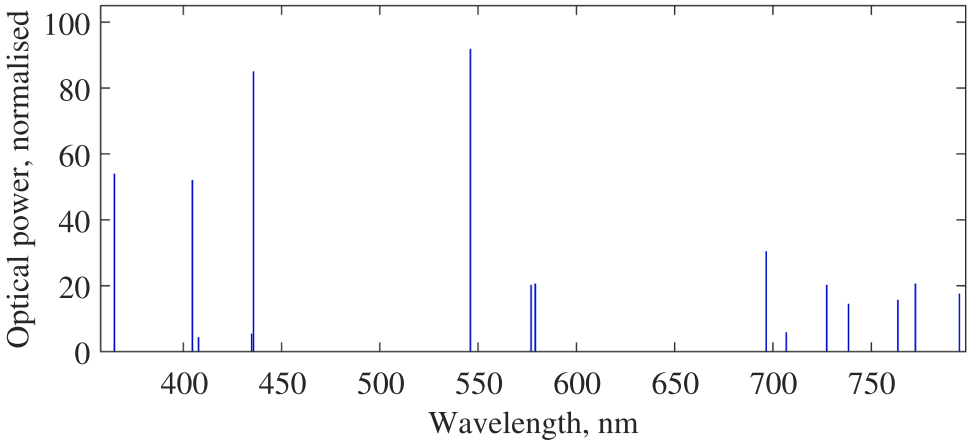

(b)

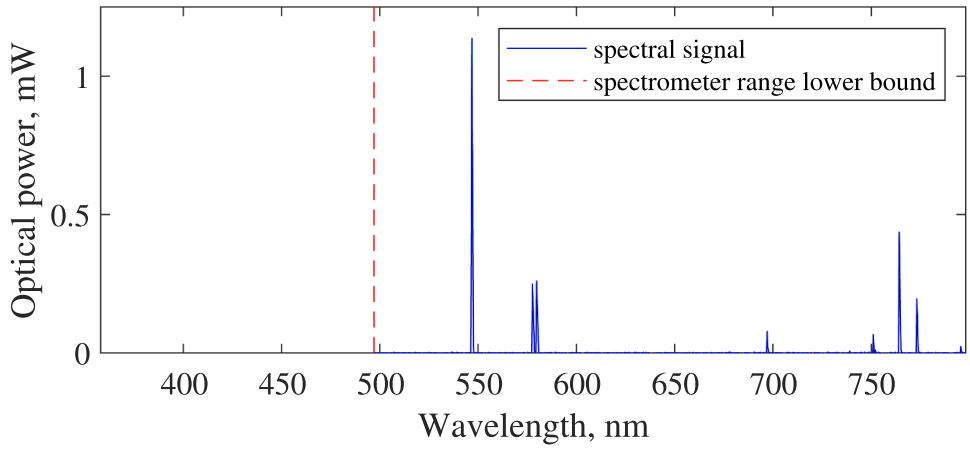

(c)

Fig. 9. Example of spectra fusing a spectral line light source: a) line spectra recorded with event-based camera, b) calibration source output and c) line spectra recorded with a compact spectrometer.

to convert output into standard units, the process is straightforward. In EB systems, because only binary information about luminance changes is available rather than quantitative values, the calibration process is far more challenging and, to our knowledge, has never been attempted before.

4. Results and analysis

For the majority of pseudo images presented in this work, the integration time was chosen to match the standard camera exposure time of $\Delta t = 33$ ms. However, to demonstrate the full capabilities of the EB camera's dynamic range, the integration time was varied, as described in Section 4.2.

4.1. Calibration light source spectra

4.1.1. Broadband light source

Radiation intensity measurements were performed using a broadband light source, and data were collected through emission spectroscopy. The tunable LED light source was used with a 5 mm diameter port, and the output luminance was set to 500 cdm/^{2}. The results reported in Fig. 8 were obtained using an integration time of $\Delta t = 33$ ms to create a pseudo image from the event stream.

The recorded broadband spectrum is shown in Fig. 8(a), while sections of the broadband spectrum are displayed in Fig. 8(b). These sections represent spectral regions of the broadband spectrum and were obtained using a range of bandpass filters with a 10 nm bandwidth. Using multiple filters helped determine the bounds of the spectral range

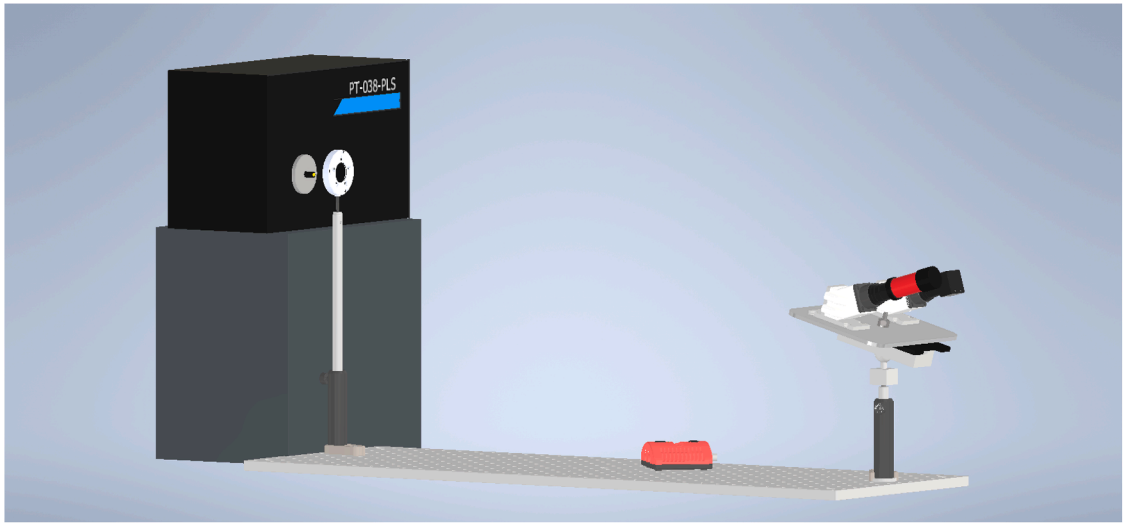

Fig. 10. Experimental setup for dynamic range tests.

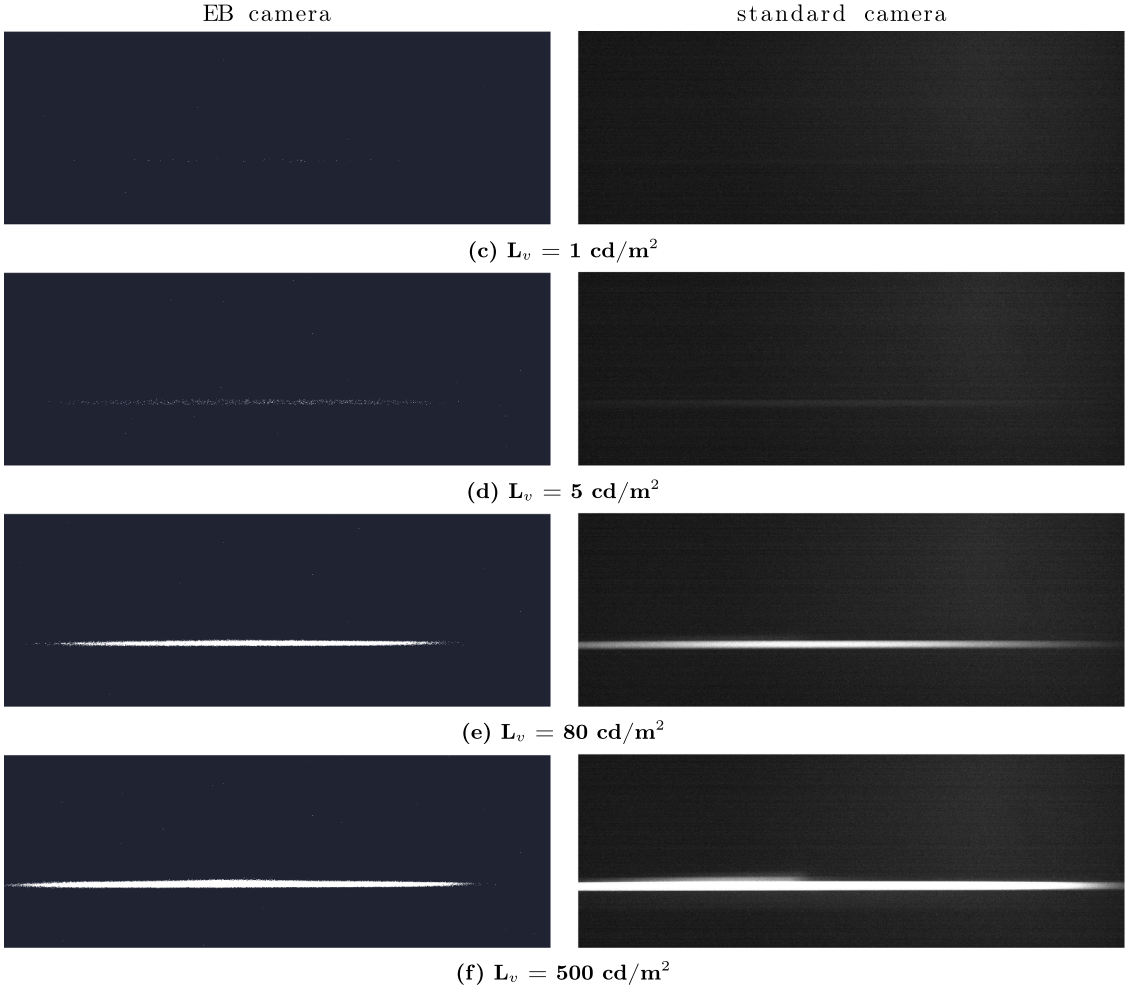

Fig. 11. Demonstration of the dynamic range for left: event-based camera spectrometer and right: standard camera spectrometer.

achieved. Both figures were created by stitching together pseudo images from different wavelength ranges to show the full wavelength range captured by the system.

To create light intensity changes with this stationary setup, the base plate holding the system was slightly shaken, which resulted in two spectral lines of different colors with a small spacing between them. In the images, the white color corresponds to “ON” events (increase in light intensity), while the blue color corresponds to “OFF” events (decrease in light intensity).

The results shown in this section demonstrate the successful basic spectroscopic capability of the instrument, specifically its ability to capture a broadband spectrum.

(a) Image

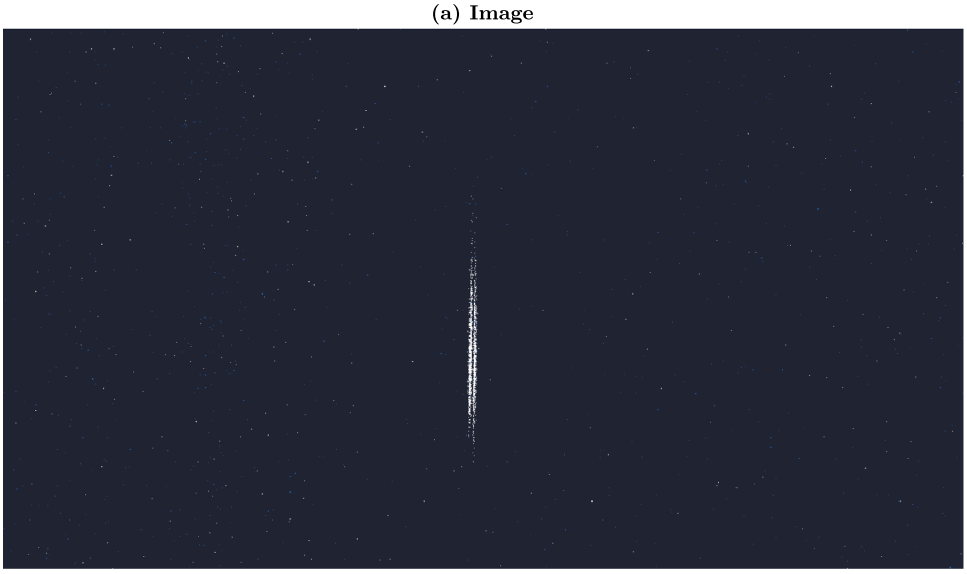

(b) Spectra

Fig. 12. Example of spectra from a flagpole beacon light, captured during daylight.

4.1.2. Spectral line light source

This set of measurements was performed using a Mercury-Argon spectral calibration source. The optical power in the 600 μm fiber was 1.6 mW. Results obtained with this light source are shown in Fig. 9 and were generated using an integration time of $\Delta t = 33$ ms to create a pseudo image from the event stream.

Fig. 9(a) illustrates the results obtained with the EB camera system. This discrete spectrum, consisting of individual spectral lines, is used for wavelength calibration of the EB camera recordings and corresponds to the output of the light source, as demonstrated in Fig. 9(b) and (c). Fig. 9(b) shows the light source output as provided by the manufacturer. The same calibration light source output was then recorded using a compact spectrometer. This spectrometer is a Thorlabs CCS175 Czerny-Turner model, covering wavelengths from 500 to 1000 nm, and was connected to the light source via a fiber optic cable to capture the emitted radiation, as shown in Fig. 9(c).

4.2. Dynamic range

To demonstrate the extended dynamic range of the event-based camera in a spectroscopy setup, the event-based and standard camera spectrometers were mounted side-by-side to record the output of a broadband light source (Labsphere PT-038-PLS) at varying luminance levels. These measurements were conducted in a dark room (i.e., with lights turned off) and with potential sources of light reflection covered. The standard camera spectrometer used settings typically employed in airborne observation missions when recording radiation from a spacecraft re-entering the Earth's atmosphere. The EB camera settings that are typically adjusted are reported in Table 3, while the others were left at the default values of the Prophesee software (Metavision® SDK version 4.5.1). The integration time for pseudo images was reduced to $\Delta t = 10\,\mu$s. This time interval was chosen because it corresponds to the average time it takes from when a row of pixels firing is read out for the first time to when the same (or a nearby) row of pixels firing is read out again. The parameters for both spectrometers are listed in Table 3.

Since the event-based camera records only when there is a change in light intensity within the field of view, an iris was used to block the light source before recording began. Once recording started, the iris was opened to allow light in. A motorized iris was employed for precise and rapid control of the aperture. Both camera systems were positioned 1 m away from the light source aperture. This setup is shown in Fig. 10.

The methodology was as follows:

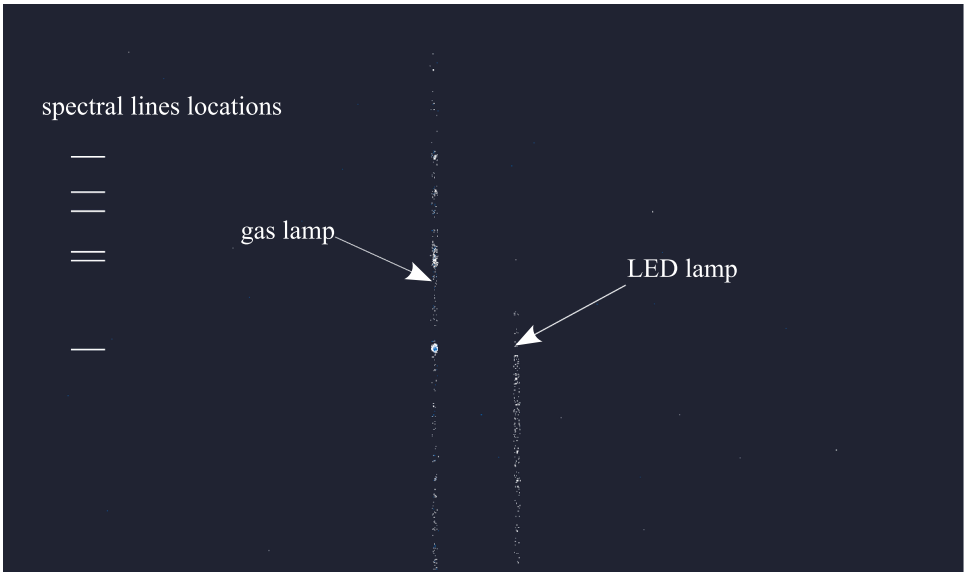

Fig. 13. Example of spectra from two different lamps.

Table 3
Summary of the camera recording properties.

Instrument	THUNDER	ASTRO
integration time [s]	$10e^{-6}$ (pseudo images)	0.033
fps	–	30
gain	–	480 (max)
bias fo	55	–
bias hpf	60	–
bias diff_on	–30	–

1. The luminance output of the light source was varied, initially in increments of 1 cd/m^2, and measurements were taken with both systems.
2. Images from the standard camera were inspected to determine whether the broadband spectrum was visible. Pseudo images from the event-based camera were also inspected, targeting the full line of the broadband spectrum.
3. If the spectrum was not detected by either system, the luminance was increased. Once the spectrum was detected, the corresponding luminance level was recorded as the lower bound for that system.
4. The luminance was then increased further, in larger increments of 10 cd/m^2. When inspection of the standard camera images showed overexposure, the previous luminance level was recorded as the upper bound for that system.
5. The luminance was increased further for the event-based system. Since event-based cameras do not produce standard images nor have exposure in the traditional sense, overexposure does not occur.

The results of this process are shown in Fig. 11. Images from both systems are presented at specific luminance levels. It can be seen that the event-based camera shows a partial spectrum already at the starting luminance level of 1 cd/m^2; however, it is not a full spectrum and thus was not deemed satisfactory. Standard camera images also show a spectrum at the lowest luminance setting; however, the signal-to-noise ratio (SNR) is too low for these to be useful. The luminance level of 5 cd/m^2 was determined to be the lower bound for both the event-based and the standard camera systems. At this level, images show full spectra with sufficient SNR to extract meaningful information.

The upper bound for the standard camera system is at 80 cd/m^2, beyond which the images become saturated. The upper bound for the event-based camera system is more difficult to determine, as intensity calibration has not yet been completed. However, we estimate it to be approximately 500 cd/m^2, where the spectrum shape begins to change slightly and deviates from the clean line shape. At this luminance, the spectrum obtained with the event-based system exhibits a small bump on the upper side.

These results indicate that while both systems share a similar lower bound, the standard camera system's upper bound is around 80 cd/m^2, whereas the event-based system's upper bound is much higher at approximately 500 cd/m^2. This large difference illustrates the extended dynamic range of the event-based camera in the spectroscopy setting. It is important to note, however, that these values are presented here for comparative purposes only. Since luminance is a photometric quantity, it would need to be converted to its analogous radiometric quantity-radiance - to accurately represent the total amount of light across all wavelengths and provide a more precise measurement of light intensity.

4.3. Daylight spectroscopy

In Section 2, the advantages of EB cameras for addressing issues related to daylight imaging of high-speed objects were explained in detail. Accordingly, the developed system was used to record the spectrum of a flagpole beacon light against a blue sky background. Fig. 12 shows the results, with the left image depicting the beacon light and the right image showing the corresponding spectra. Fig. 12(a) was obtained using a standard color camera (Sony Cyber-shot DSC-RX100) to provide a reference image for the spectra, while Fig. 12(b) is a pseudo image created by integrating the event stream over $\Delta t = 33$ ms. Note that the beacon has two LED lights, which is why two closely spaced spectral lines appear in Fig. 12.

Fig. 12 demonstrates that the EB camera system is capable of capturing the spectra of objects viewed against a clear sky. The beacon light is an LED with a red filter, and based on the system's spectral resolution, the captured spectrum spans approximately 30 nm in the red wavelength region.

4.4. Long range spectroscopy

Fig. 13 shows examples of spectra obtained from two different types of streetlights: a gas-type lamp and an LED-type lamp. LED streetlights produce a broad-spectrum "white" light, while gas-type lamps emit discrete spectra with spectral lines corresponding to the specific gas used. Based on these characteristics, we identified the spectrum on the left

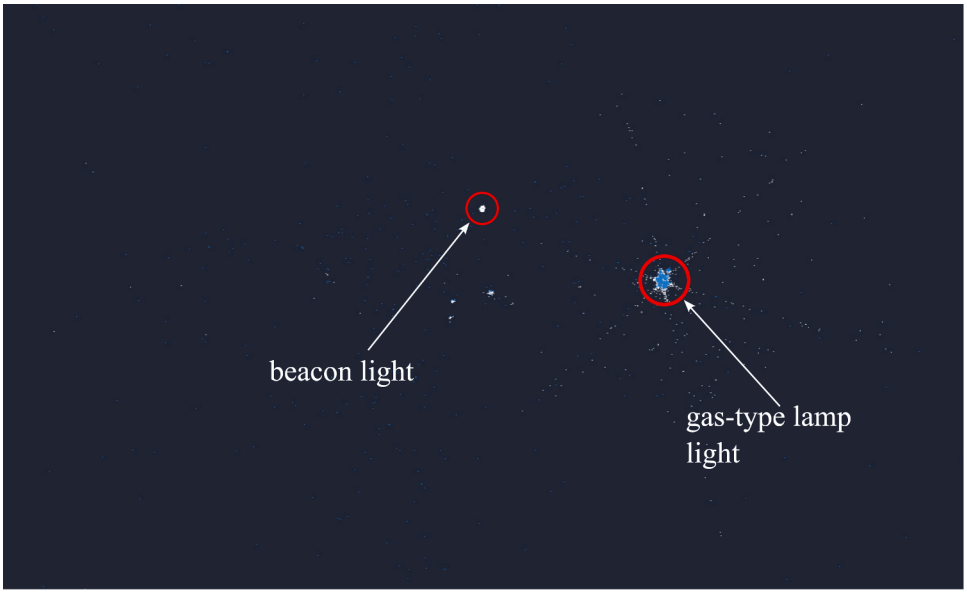

(a) Image

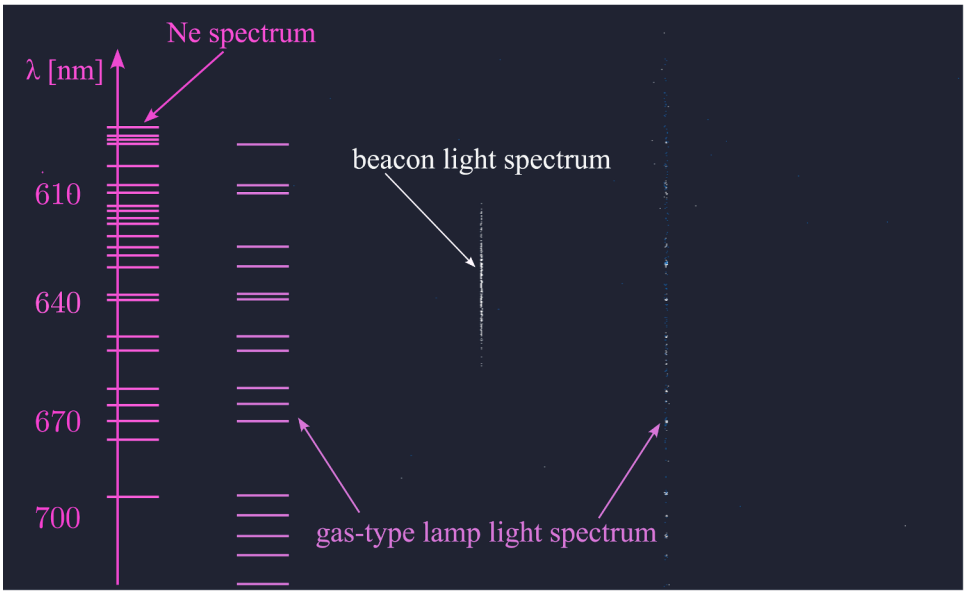

(b) Spectra

Fig. 14. Example of spectra from two different lights at over 5 km distance, captured during nighttime.

as originating from a gas lamp, as indicated by bright spectral lines superimposed on a continuous background. In contrast, the spectrum on the right, which is continuous without discrete lines, corresponds to an LED-type lamp. The positions of the spectral lines from the gas-type lamp were identified and are marked with red horizontal lines in the figure. These spectra were recorded from a distance of several hundred meters from the light sources.

However, since objects typically observed during hypersonic flight events are located at distances of at least several tens of kilometers from the recording instruments, the spectrum was imaged from the same flagpole beacon light as before, but at a greater distance of approximately 7 km. The result is shown in Fig. 14, which presents a discrete spectrum composed of distinct spectral lines, indicating that the source is a gas-type lamp.

This figure shows the same red portion of the wavelength region as in Fig. 12, as the spectrum originates from the same beacon light previously discussed in Section 4.3. The positions of the spectral lines from the gas-type lamp were identified and are marked with horizontal lines in the figure.

Given the typical orange-red color of the light output, the lamp is most likely a neon lamp, which emits radiation in the 600–700 nm range. For comparison, the discrete spectrum of neon gas, with known spectral line wavelengths, has been overlaid. Based on this comparison, we conclude that the gas-type lamp spectrum most closely matches that of neon. This also allows us to identify that the beacon light spectrum lies in the wavelength range of approximately 620–650 nm.

5. Conclusion

The work presented here demonstrates the viability of pairing EB cameras with a diffraction grating to record spectra. Measurements with this neuromorphic system were performed using a range of light sources and conditions. The results show that the designed system is capable of capturing both broadband and line spectra. By comparing the recorded

spectra with known source data and manufacturer specifications, it was possible to identify specific spectral lines of Hg and Ar.

Dynamic range, daylight, and long-range spectroscopy results show improved performance of the EB system compared to a standard camera. Qualitative comparisons indicate a significantly higher dynamic range of the EB camera system when using settings typical for hypersonic flight radiation measurements. Daylight spectroscopy results confirm the system's ability to record spectra against a clear sky background, while long-range results demonstrate its capability to capture spectra from distances of several kilometers.

The results from these test cases provide confidence in the potential of neuromorphic spectroscopy for collecting hypersonic flight data. The intensity calibration component of this study is ongoing, and additional results will be reported in a future publication.

Additionally, although the current focus of the proposed neuromorphic spectroscopy system is on airborne observation of prototype flight vehicles and re-entry objects, its potential applications extend further. This novel sensor could also be used for monitoring commercial aircraft exhaust emissions, aligning with efforts to track harmful gas outputs. Furthermore, the developed technology could be adapted for remote optical diagnostics in future land-based, semi-autonomous vehicles for on-board sensing.

CRediT authorship contribution statement

Tamara Sopek: Writing – review & editing, Writing – original draft, Visualization, Validation, Software, Resources, Project administration, Methodology, Investigation, Funding acquisition, Formal analysis, Data curation, Conceptualization; **Fabian Zander:** Writing – review & editing, Supervision, Funding acquisition, Conceptualization; **Byrenn Birch:** Writing – review & editing, Methodology, Investigation; **David Buttsworth:** Writing – review & editing, Supervision, Funding acquisition, Conceptualization.

Data availability

Data will be made available on request.

Declaration of competing interest

The authors declare that they have no known competing financial interests or personal relationships that could have appeared to influence the work reported in this paper.

Acknowledgements

The authors would like to acknowledge the loan of the DVXplorer Lite EB cameras from Duncan Wright that were used for the initial work with these types of cameras and before we acquired a Prophesee EVK4.

References

[1] D. Harland, R. Lorenz, Space Syst. Fail., 2005.
[2] J. Li, X. Liu, H. Li, Z. Yu, Z. Li, J. Liu, Image analysis for the fault diagnosis in a rocket engine failure, in: 2nd Target Recognition and Artificial Intelligence Summit Forum, 2020. https://doi.org/10.1117/12.2548972
[3] R. MItchell, Space shuttle solid rocket booster redesign and testing, in: Progress in Space Transportation, 1989.
[4] M. Melis, K. Carney, J. Gabrys, E. Fasanella, K. Lyle, A summary of the space shuttle Columbia tragedy and the use of LS dyna in the accident investigation and return to flight efforts, in: 8th International LS-DYNA Users Conference, 2004.
[5] NASA Independent Review Team, SpaceX CRS-7 Accident Investigation Report, Technical report, NASA, ????
[6] J. Dinner, SpaceX reveals why its Starship Flight 8 Ship exploded, failure traced to 'flash' in rocket's engines, 2025. https://www.space.com/space-exploration/private-spaceflight/spacex-knows-why-its-starship-flight-8-ship-exploded-traced-to-flash-in-rocket-engines?utm_source=chatgpt.com.
[7] Lou M., and Griggs B., NASA wants to land astronauts on Mars by 2033, 2019. https://edition.cnn.com/2019/04/03/us/nasa-mars-mission-2033-scn-trnd/, accessed 20 November, 2023.
[8] NASA, Humans to Mars, 2025. https://www.nasa.gov/humans-in-space/humans-to-mars/.
[9] A. Mazaheri, C. Johnston, Shock-layer radiative heating for MSR sample retrieval lander with 8 km/s entry, in: 3rd International Conference on Flight Vehicles, Aerothermodynamics and Re-entry (FAR), 2025.
[10] A.M. Brandis, C.O. Johnston, M. Panesi, B.A. Cruden, D. Prabhu, Investigation of nonequilibrium radiation for Mars entry, in: 51st AIAA Aerospace Sciences Meeting Including the New Horizons Forum and Aerospace Exposition, 2013. https://doi.org/10.2514/6.2013-1055
[11] A. Tibère-Inglesse, C.O. Johnston, A.M. Brandis, B.A. Cruden, Examination of Mars2020 shock-layer conditions via infrared emission spectroscopy of CO_2, in: AIAA Aviation Forum, 2023. https://doi.org/10.2514/6.2023-0960
[12] Z. Jiang, Z. Hu, Y. Wang, G. Han, Advances in critical technologies for hypersonic and high-enthalpy wind tunnel 33 (12) (2020) 3027–3038. https://doi.org/10.1016/j.cja.2020.04.003
[13] Z. Jiang, H. Yu, Theories and technologies for duplicating hypersonic flight conditions for ground testing 4 (3) (2017) 290–296. https://doi.org/10.1093/nsr/nwx007
[14] A.M. Brandis, B.A. Cruden, Titan atmospheric entry radiative heating, in: 47th AIAA Thermophysics Conference, 2017. AIAA 2017–4534. https://doi.org/10.2514/6.2017-4534
[15] T. Sopek, A. Glenn, J. Clarke, L. Di Mare, P. Collen, M. McGilvray, Radiative heat transfer measurements of Titan atmospheric entry in a shock tube, J. Thermophys. Heat Transf. (2024). Accepted for publication.
[16] S. Löhle, A. Meindl, E. Poloni, J. Steer, T. Sopek, M. McGilvray, L. Walpot, Experimental simulation of gas giant entry in the PWK1 arcjet facility including CH4, in: AIAA SciTech Forum 2022, 2022. AIAA 2022-0264. https://doi.org/10.2514/6.2022-0264
[17] A. Gülhan, D. Hargarten, M. Zurkaulen, F. Klingenberg, F. Siebe, S. Willems, G. Di Martino, T. Reimer, Selected results of the hypersonic flight experiment STORT 211 (2023) 333–343. https://doi.org/10.1016/j.actaastro.2023.06.034
[18] P. Jenniskens, J. Albers, M.W. Koop, M.S. Odeh, K. Al-Noimy, K. Al-Remeithi, K. Al Hasmi, R.F. Dantowitz, F. Gasdia, S. Löhle, F. Zander, T. Hermann, D. Farnocchia, S.R. Chesley, P.W. Chodas, R.S. Park, J.D. Giorgini, W.J. Gray, D.K. Robertson, T. Lips, Airborne observations of an asteroid entry for high fidelity modeling: space debris object WT1190f, in: AIAA Science and Technology Forum and Exposition, 2016. AIAA 2016-0999. https://doi.org/10.2514/6.2016-0999
[19] M. Jenniskens, P. Gural, L. Dynneson, B. Grigsby, K. Newman, M. Borden, M. Koop, D. Holman, CAMS: Cameras for Allsky Meteor Surveillance to establish minor meteor showers, Icarus 216 (2011) 40–61. https://doi.org/10.1016/j.icarus.2011.08.012
[20] T.J. McIntyre, R. Khan, T.N. Eichmann, B. Upcroft, D. Buttsworth, Visible and near infrared spectroscopy of Hayabusa reentry using semi-autonomous tracking, J. Spacecr. Rock. 51 (1) (2014) 31–36. https://doi.org/10.2514/1.A32497
[21] J. Tóth, L. Kornoš, P. Zigo, S. Gajdoš, D. Kalmančok, J. Világi, J. Šimon, P. Vereš, J. Šilha, M. Buček, A. Galád, P. Rusňák, P. Hrábek, F. Ďuriš, R. Rudawska, All-sky meteor orbit system AMOS and preliminary analysis of three unusual meteor showers, The Astrophys. J. Supplem. Ser. 93 (1) (2015) 351–395. https://doi.org/10.1016/j.pss.2015.07.007
[22] F. Zander, D. Buttsworth, B. Birch, L. Noller, D. Wright, C. James, M. Thompson, S. Apirana, J. Leis, C. Lobsey, A. Payne, Australian rapid-response airborne observation of the Hayabusa2 reentry, J. Spacecr. Rock. 58 (6) (2021) 1915–1919. https://doi.org/10.2514/1.A35062
[23] B. Birch, F. Zander, D. Buttsworth, L. Noller, A. Payne, Hayabusa2 capsule reentry: Australian airborne observation emission spectroscopy calibration and preliminary analysis, in: AIAA SciTech Forum, 2022. AIAA 2022–2151. https://doi.org/10.2514/6.2022-2151
[24] F. Zander, B. Birch, D. Buttsworth, A. Payne, Planning and implementation of the Australian airborne observation of Hayabusa2, in: AIAA Aviation Forum, 2022. AIAA 2022–3583. https://doi.org/10.2514/6.2022-3583
[25] B. Birch, F. Zander, D. Buttsworth, L. Noller, A. Payne, Hayabusa2 capsule reentry: visible and near-IR emission spectroscopy from the Australian airborne observation, in: AIAA Aviation Forum, 2022. AIAA 2022–3736. https://doi.org/10.2514/6.2022-3736
[26] R. Schwartz, T. Horvath, T. Pepp, Scientifically calibrated in-flight imagery (SCIFLI) mission operations for the SpaceX CRS-4 airborne infrared imaging, in: AIAA Space Forum, 2017. AIAA 2017–5209. https://doi.org/10.2514/6.2017-5209
[27] T. Spisz, J. Taylor, D. Gibson, S. Kennerly, K. Osei-Wusu, G. Scriven, T. Pottebaum, T. Horvath, R. Schwartz, S. Tack, B. Bush, Processing infrared imagery of the SpaceX Falcon first stage reentry during CRS-4 mission, in: AIAA Space Forum, 2017. AIAA 2017–5209. https://doi.org/10.2514/6.2017-5293
[28] C. Scott, J. Inman, SCIFLI Airborne observation of the Hayabusa2 sample return capsule re-entry, in: AIAA Aviation Forum, 2022. AIAA 2022–3798. https://doi.org/10.2514/6.2022-3798
[29] B. McReynolds, R. Graca, D. O'Keefe, R. Oliver, R. Balthazor, N. George, M. McHarg, Modeling and decoding event-based sensor lightning response, in: Unconventional Imaging, Sensing, and Adaptive Optics, 2023. 1269313. https://doi.org/10.1117/12.2674435
[30] C. Benson, M. Holzinger, Simulation and analysis of event camera data for non-resolved objects 71 (3) (2023). https://doi.org/10.1007/s40295-023-00423-6
[31] M. Nishiguchi, C. Frueh, B. McReynolds, Event-based vision sensor physics-based digital twin for tuning SSA use, in: Advanced Maui Optical and Space Surveillance Technologies Conference (AMOS), 2024.
[32] X. Mou, R. Jiang, W. Zhang, M. Guo, B. Mu, A. Suess, Joint parameter estimation for event-based vision sensor characterization, in: Electronic Imaging, 2024, pp. 289-1–289-5. https://doi.org/10.2352/EI.2024.36.7.ISS-289

[33] N. Zubić, M. Gehrig, D. Scaramuzza, State space models for event cameras, in: The IEEE/CVF Conference on Computer Vision and Pattern Recognition, 2024, pp. 5819–5828.
[34] S. Afshar, A.P. Nicholson, A. van Schaik, G. Cohen, Event-based object detection and tracking for space situational awareness, IEEE Sens. J. 20 (24) (2020) 15117–15132. https://doi.org/10.1109/JSEN.2020.3009687
[35] G. Gallego, T. Delbrück, G. Orchard, C. Bartolozzi, B. Taba, A. Censi, S. Leutenegger, A. Davison, J. Conradt, K. Daniilidis, D. Scaramuzza, Event-based vision: a survey, IEEE Trans. Pattern Anal. Mach. Intell. 44 (1) (2020) 154–180. yhttps://doi.org/10.1109/TPAMI.2020.3008413
[36] T. Delbrück, M. Lang, Robotic goalie with 3ms reaction time at 4CPU load using event-based dynamic vision sensor, Front. Neurosci. 7 (2013). . https://doi.org/10.3389/fnins.2013.00223
[37] G. Orchard, C. Meyer, R. Etienne-Cummings, C. Posch, N. Thakor, R. Benosman, HFirst: A temporal approach to object recognition, IEEE Trans. Pattern Anal. Mach. Intell. 37 (10) (2015) 2028–2040. https://doi.org/10.1109/TPAMI.2015.2392947
[38] D. Borer, T. Delbrück, T. Rösgen, Three-dimensional particle tracking velocimetry using dynamic vision sensors, Exp. Fluid. 58 (165) (2017) 1–7. https://doi.org/10.1007/s00348-017-2452-5
[39] G. Cohen, S. Afshar, A. van Schaik, A. Wabnitz, T. Bessell, M. Rutten, B. Morreale, Event-based sensing for space situational awareness, in: The Advanced Maui Optical and Space Surveillance (AMOS) Technologies Conference, 2017.
[40] K. Boahen, A burst-mode word-serial address-event link-I: transmitter design, IEEE Transact. Circuit. Syst.-I: Regul. Pap. 51 (7) (2004) 1269–1280. https://doi.org/10.1109/TCSI.2004.830703
[41] T. Finateu, A. Niwa, D. Matolin, K. Tsuchimoto, A. Mascheroni, E. Reynaud, P. Mostafalu, F. Brady, L. Chotard, F. LeGoff, H. Takahashi, H. Wakabayashi, Y. Oike, C. Posch, A 1280x720 back-illuminated stacked temporal contrast event-based vision sensor with 4.86 μm pixels, 1.066GEPS readout, programmable event-rate controller and compressive data-formatting pipeline, in: 2020 IEEE International Solid-State Circuits Conference - (ISSCC), 2020, pp. 112–114. https://doi.org/10.1109/ISSCC19947.2020.9063149
[42] S.A. P., Knowledge center, (2024). https://www.prophesee.ai/, accessed on 05 Jul 2024.
[43] P. Lichtsteiner, C. Posch, T. Delbrúck, A 128×128×120 dB 15 μs latency asynchronous temporal contrast vision sensor, IEEE Journal of Solid-State Circuit.: Regul. Pap. 43 (2) (2008) 1269–1280. https://doi.org/10.1109/JSSC.2007.914337
[44] Y. Suh, S. Choi, M. Ito, J. Kim, Y. Lee, J. Seo, H. Jung, D.-H. Yeo, S. Namgung, J. Bong, J.s. Kim, P.K.J. Park, J. Kim, H. Ryu, Y. Park, A 1280×960 dynamic vision sensor with a 4.95-μm pixel pitch and motion artifact minimization, in: 2020 IEEE International Symposium on Circuits and Systems (ISCAS), 2020, pp. 15117–15132. https://doi.org/10.1109/ISCAS45731.2020.9180436
[45] M. Aitsam, S. Davies, A. Di Nuovo, Event camera-based real-time gesture recognition for improved robotic guidance, in: International Joint Conference on Neural Networks (IJCNN), IEEE, 2024.
[46] P. Shi, C.-O. Chow, W. Wong, Fusion techniques of frame and event cameras in autonomous driving: a review, Inform. Fus. 127 (A) (2026). 103697. https://doi.org/10.1016/j.inffus.2025.103697
[47] E. Piatkowska, A. Belbachir, S. Schraml, M. Gelautz, Spatiotemporal multiple persons tracking using dynamic vision sensor, in: IEEE Conf. Comput. Vis. Pattern Recog. Workshops (CVPRW), 2012.
[48] W. Chamorro, J. Andrade-Cetto, J. Sola, High-speed event camera tracking, in: The 31st British Machine Vision Virtual Conference, 2020.
[49] P. Jenniskens, Observations of the stardust sample return capsule entry with a slitless echelle spectrograph, J. Spacecr. Rock. 47 (5) (2010) 718–735. https://doi.org/10.2514/1.37518
[50] D. Buttsworth, R. Morgan, P. Jenniskens, Near-ultraviolet emission spectroscopy of the Hayabusa reentry, J. Spacecr. Rock. 50 (6) (2013) 1109–1120. https://doi.org/10.2514/1.A32500
[51] S. Löhle, F. Zander, S. Lemmens, H. Krag, Airborne observations of re-entry breakup: results and prospects, in: 7th European Conference on Space Debris, 2017. SDC7 paper 410.